RSC Advances

ROYAL SOCIETY OF CHEMISTRY

www.rsc.org/advances

Journal Name

RSCPublishing

ARTICLE

Magnetically Separable $ZnFe_2O_4$, $Fe_2O_3/ZnFe_2O_4$ and $ZnO/ZnFe_2O_4$ Hollow Nanospheres with Enhanced Visible Photocatalytic Property

Cite this: DOI:

Received 00th
Accepted 00th

DOI:

www.rsc.org/

Junqi Li*, Zhenxing Liu, Zhenfeng Zhu

Magnetically separable $ZnFe_2O_4$-based composite hollow nanospheres with dimension of 230 nm were successfully synthesized via impregnating-calcination process using phenolic formaldehyde nanospheres (PFS) as template. $ZnFe_2O_4$, $Fe_2O_3/ZnFe_2O_4$ and $ZnO/ZnFe_2O_4$ hollow nanospheres were synthesized by tuning the concentration of zinc salts. The samples were characterized by X-ray powder diffraction, energy dispersion spectroscopy, scanning electronic microscopy, transmission electron microscopy, nitrogen sorption measurement, UV-vis diffuse reflectance spectra and photoluminescence emission spectra. The results of photodegradation under visible light irradiation exhibited the order: $ZnO/ZnFe_2O_4$ > $Fe_2O_3/ZnFe_2O_4$ > $ZnFe_2O_4$ > bulk $ZnFe_2O_4$, and close investigation revealed that the high surface area, thin shell thicknesses, and matching heterostructure of the as-prepared $ZnO/ZnFe_2O_4$ and $Fe_2O_3/ZnFe_2O_4$ composites could dramatically improve the photocatalytic activities, which facilitates the efficient separation of photoinduced electron-hole pairs. Furthermore, the $ZnFe_2O_4$-based hollow nanospheres could be conveniently separated by using an external magnetic field, and be chemically and optically stable after several repetitive tests. The study also provides a general and effective method in the composition-tunable hollow nanomaterials with sound heterojunctions that may show a variety of applications.

1. Introduction

Nowadays, functional nanomaterials with controlled shapes and desired morphology are of great importance in the application of the photocatalyst, because of their unique chemical and physical properties with conspicuous enhanced photocatalytic property compared to their bulk counterparts [1]. Hollow nanomaterials with remarkable interior space have been intensively investigated because of their low density, larger specific surface area and nanostructured wall. By far, the templated method is one of the most effective methods in the preparation of hollow spheres. The performance of as-formed hollow spheres is determined by the physical and chemical properties of the template, such as their shape, size, porosity, functional group, and surface charge. Hollow spheres by templates method in the adsorption of cationic metal ions has already been demonstrated [2].

Nanomaterials are effective to enhance the photocatalytic activities by minimizing the particle size, so as to achieve higher surface area and more active catalytic sites compared to their bulk counterparts, but it brings another negative effect. When the particle size is decreased to nanoscale, the separation and the recycling of the photocatalysts from the treated water are practical obstacles, which hinders their application in industrial use, even though they have high photocatalytic activity. Thus, some researchers are working on magnetic photocatalysts that can be separated from the treating system by applying an external magnetic field [3]. Spinel-structured $ZnFe_2O_4$ nanoparticles with strong magnetism, outstanding photochemical stability and low cost, as well as a narrow bandgap about 1.9 eV, which give rise to the visible-light response, have become increasingly attractive in the area of photocatalysis [4-8]. However, as single phase photocatalysts, their activity is low. Combining two or more semiconductors with appropriate band positions to improve the photocatalytic performance of the semiconductors is an established idea,

*School of Materials Science and Engineering, Shaanxi University of Science and Technology, Xi'an 710021, PR China, Email: sfmlab@163.com, Tel: +86-29-86177018 Fax: +86-29-86177018

because it can lead to an enhanced charge separation efficiency and enlonged charge carrier life. Recently, some materials have been applied to prepare heterojunction structures together with $ZnFe_2O_4$ to enhance the photoelectric conversion efficiency, such as $CaFe_2O_4$ [9], TiO_2 [10,11], $SrFe_{12}O_{19}$ [12] and Ag_3VO_4 [13]. Traditional method to prepare composite is complex. The first step is to prepare the matrix of composite, and then decorates the matrix phase via a series of complicated process, so as to achieve the effect of the composite [14,15]. However, in our research, we can synthesize $ZnFe_2O_4$-based composite hollow nanospheres (such as $Fe_2O_3/ZnFe_2O_4$ and $ZnO/ZnFe_2O_4$) via impregnating-calcination process by tuning the amounts of zinc salts with the same procedure [16].

In this work, the synthesis, characterization and photocatalytic results of RhB degradation using $ZnFe_2O_4$-based hollow nanospheres with visible light radiation is reported, and $ZnFe_2O_4$, $Fe_2O_3/ZnFe_2O_4$ and $ZnO/ZnFe_2O_4$ hollow nanospheres were synthesized by tuning the concentration of zinc salts. These results of RhB degradation were compared with the bulk $ZnFe_2O_4$. And the enhanced photochemical behaviors of the $Fe_2O_3/ZnFe_2O_4$ and $ZnO/ZnFe_2O_4$ hollow nanospheres are also discussed in detail.

2. Experimental

2.1 Synthesis of PFS, $ZnFe_2O_4$-based hollow nanospheres and bulk $ZnFe_2O_4$

Preparation of phenolic formaldehyde microspheres (PFS). Typically, monodisperse PFS were synthesized by using resorcinol and formaldehyde solution as precursors. In a typical synthesis of the PFS, ammonia aqueous solution (NH_4OH, 0.1 mL, 25 wt %) was mixed with a solution containing absolute ethanol (EtOH, 8 mL) and deionized water (H_2O, 20 mL), then stirred for more than 1 h. Subsequently, resorcinol (0.2 g) was added and continually stirred for 30 min. The formaldehyde solution (0.28 mL) then added to the reaction solution and stirred for 12 h at 30 °C, and subsequently heated for 24 h at 100 °C under a static condition in a Teflon-lined autoclave. The solid product was recovered by centrifugation and air-dried at 50 °C for 24 h [17].

Preparation of $ZnFe_2O_4$, $Fe_2O_3/ZnFe_2O_4$ and $ZnO/ZnFe_2O_4$ hollow nanospheres. $ZnFe_2O_4$(S1) hollow nanospheres were synthesized by impregnating-calcination process. 20 mL solution with 1 M $Zn(NO_3)_2$ and 2 M $Fe(NO_3)_3$ was added into a 100 mL flask and dissolved to form a clear solution with strong stirring; 0.5 g of the as-prepared PFS were added and dispersed into this solution with the aid of ultrasonication. After ultrasonic dispersion for 15 min, the resulting suspension was aged for 3 h at room temperature, then filtered, washed, and dried at 50 °C for 24 h. The resultant composite microspheres were heated in air at 1 °C min^{-1} up to 650 °C, kept this temperature for 3 h, and cooled naturally to room temperature. $ZnO/ZnFe_2O_4$(S2) and $Fe_2O_3/ZnFe_2O_4$(S3) hollow nanospheres were synthesized by changing $Zn(NO_3)_2$ concentration with 1.5 M and 0.5 M, and they were also synthesized by following the same procedure, and the synthetic conditions were summarized in Table 1.

Preparation of bulk $ZnFe_2O_4$. 20 mL solution with 1 M of $Zn(NO_3)_2$ and 2 M of $Fe(NO_3)_3$ was added into a 100 mL flask and dissolved to form a clear solution with strong stirring, and then dried at 50 °C for 48 h. The resultant samples were heated in air at 1 °C min^{-1} up to 650 °C, kept this temperature for 3 h, and cooled naturally to room temperature.

2.2 Characterization

X-ray diffractometry (XRD-D/max 2200pc, Japan) with Cu Kα radiation of wavelength λ = 0.154 nm was used to verify crystal phase. The morphologies and microstructures of the samples were observed by high-resolution field emission environmental scanning electron microscope (FE-SEM, Hitachi S-4800) and transmission electron microscopy (TEM) (JEM-2100). And the energy dispersive X-ray analysis of the samples weres also investigated during the FE-SEM measurements. The optical diffuse reflectance spectra was carried out with a UV-2550 UV-vis spectrophotometer (Shimadzu, Japan) using $BaSO_4$ as reference. Moreover, the photoluminescence spectra was examined with an F-4600 fluorescence spectrophotometer (Hitachi F-4500, Japan). The porosity and adsorption performance of the products were determined via NOVA 2200e nitrogen adsorption apparatus.

2.3 Measurements of photocatalytic activities and photoelectrochemical characterization

Photocatalytic activities of all samples were evaluated in terms of the photodecomposition of RhB aqueous solution as a standard pollutant under simulated solar light irradiation, and a 500 W Xe lamp equipped with a UV cutoff filter (λ> 420 nm) was used as a light source to cool the lamp. Prior to illumination, the suspensions containing 20 mg of the as-prepared photocatalysts and 20 mL of RhB solution (10 mg/L) in a quartz tube were sonicated for 15 min and then stirred for 30 min in the dark to ensure the adsorption-desorption equilibrium between the photocatalyst and RhB solution. Subsequently the suspensions were exposed to Xe lamp light irradiation under magnetic stirring until RhB solution was colourless. At given time intervals, a certain amount of suspension in the test tube was sampled and centrifugated to remove the photocatalyst powders. Then the supernatant solution was decanted and the UV-visible absorption spectra was monitored using a Shimadzu UV-2550 UV-vis spectrophotometer.

Photocurrent density was detected using a CHI660D electrochemical workstation with a standard three-electrode configuration containing the as-prepared samples as the working electrode, a platinum wire as the counter electrode, and the Ag/AgCl (3 M KCl) as reference electrode. 1 M NaOH electrolytes in a 100 mL glass beaker was employed as the electrolyte and a 300 W Xe lamp was used as a light source. Besides, the working electrodes of ZnFe2O4-based composites were prepared with a scrape-coating method according to a reported method [18].

3. Results and discussion

3.1 Formation of $ZnFe_2O_4$-based hollow nanospheres

Generally, template-assisted synthesis of hollow structure using PFS is based on the adsorption of metal ions on the surface layer of the microspheres, mainly depending on the electrostatic interaction and coordination with surface hydroxyl groups, and few metal ions could reach the inside of the microspheres, since the size of the pore within the microspheres is very small. A schematic for the formation of $ZnFe_2O_4$-based hollow nanospheres is given in Figure 1, the first step is that PFS impregnate in metal salt solution and PFS adsorb Zn^{2+} and Fe^{3+} on the surface. Zn^{2+} and Fe^{3+} ions are usually no larger than 20 nm decorating on the surface of PFS. In the process of heating, the $ZnFe_2O_4$ precursor shows a complicated process, in the range of 105-350 °C attribution to elimination of bound water and the conversion of residual nitrates to ZnO and Fe_2O_3. As the further heat, reactions could happen for the formation of $ZnFe_2O_4$ between ZnO and Fe_2O_3 during the calcination process, and with carbon microspheres thermal decomposition. The process could be presented by reaction 1-4 as follows:

$$Zn(NO_3)_2 \text{——} ZnO + NO_2\uparrow + O_2\uparrow \quad (1)$$

$$Fe(NO_3)_3 \text{——} Fe_2O_3 + NO_2\uparrow + O_2\uparrow \quad (2)$$

$$ZnO + Fe_2O_3 \text{——} ZnFe_2O_4 \quad (3)$$

$$C_mH_n \text{——} CO_2 + H_2O \quad (4)$$

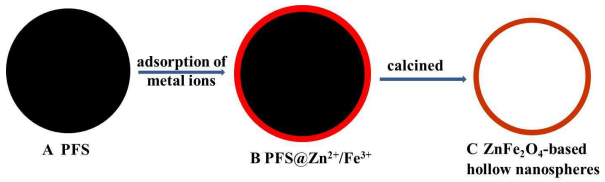

Figure 1. Schematic illustration of the formation of $ZnFe_2O_4$-based hollow nanospheres.

3.2 XRD analysis

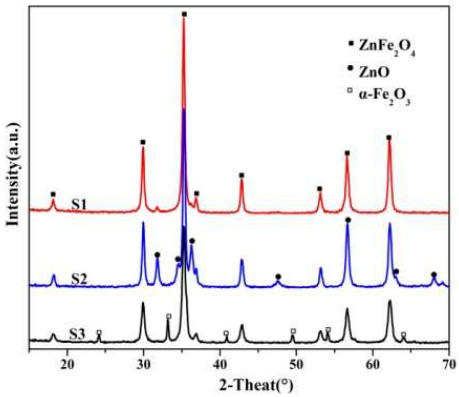

Figure 2. XRD patterns of $ZnFe_2O_4$-based composite: (S1) $ZnFe_2O_4$, (S2) $ZnO/ZnFe_2O_4$, (S3) $Fe_2O_3/ZnFe_2O_4$.

The phase of $ZnFe_2O_4$-based composites is identified by XRD characterization in Figure 2. The peaks located at 31.58°, 34.30°, 36.08°, 47.58°, 56.44°, 62.40°, 66.98°, 68.08°, and 68.84 ° are ascribed to the characteristic peaks of the hexagonal phase of ZnO (JCPDS No. 36-1451). The peaks located at 18.20°, 29.93°, 35.30°, 36.82°, 42.90°, 46.95°, 53.17°, 56.69°, 62.25°, and 73.50° can be readily ascribed to the characteristic peaks of the cubic phase of $ZnFe_2O_4$ (spinel ferrite). The XRD patterns of the sample located at 24.16°, 33.18°, 35.26°, 42.90°, 49.50°, 53.20° 62.28° and 64.08° are corresponded to α-Fe_2O_3(JCPDS No. 33-0664). The intense and sharp peaks elucidate that $ZnFe_2O_4$-based composites are well-crystallized, and from curve S1, we can find impurity of ZnO in $ZnFe_2O_4$.

3.3. Composition analysis

Table 1. Synthesis conditions and compositions for different ferrite hollow spheres.

sample	metal ion concn (M)	phase[a]	molar ratios of Zn:Fe[b]
S1	C_{Zn2+}=1, C_{Fe2+}=2	$ZnFe_2O_4$	0.480
S2	C_{Zn2+}=1.5, C_{Fe2+}=2	$ZnO/ZnFe_2O_4$	0.775
S3	C_{Zn2+}=0.5, C_{Fe2+}=2	$Fe_2O_3/ZnFe_2O_4$	0.255

[a] Determined by XRD analysis. [b] Determined by EDS analysis

The energy dispersion spectroscopy (EDS) analysis has been carried out to examine the chemical composition of $ZnFe_2O_4$-based nanospheres. As shows in Figure 3, peaks of Fe, Zn, O elements are detected, and no other impurities can be observed. EDS results show that the molar ratio of Zn to Fe is 0.48, which is close to our designed value of 0.5. And $ZnO/ZnFe_2O_4$ and $Fe_2O_3/ZnFe_2O_4$ are summarized in Table 1.

Previously, hollow spheres of various single-metal oxides have been easily synthesized by using carbonaceous saccharide spheres as templates. However, this method could not be extended from single-metal oxides to binary-metal oxides, since the difference of adsorption ability of functional groups to different metal ions makes it difficult to precisely control the molar ratio of both metal elements in the resultant product and often result in an impurity phase. In our experiment, homogeneous hollow nanospheres of pure ferrites could be obtained, and we think this can be influenced by the high concentration of metal salt. So we can confirm the process provides an easy and effective method in the fabrication of composites [19].

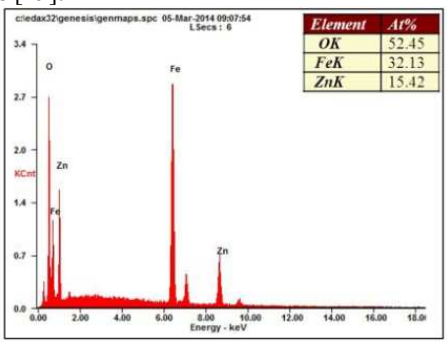

Figure 3. Energy-dispersive X-ray analysis (EDX) of the $ZnFe_2O_4$ composite.

3.4. Morphology characterization

PFS were prepared from formaldehyde and resorcinol under hydrothermal conditions at 100 °C. The narrow size distributions of the final products are demonstrated by SEM (Figure 4a). The high-magnification SEM image (Figure 4b)

and dynamic light scattering (DLS) demonstrates that these PFS have smooth surfaces and a mean diameter of 510 nm. From figure 4, we can easily associate PFS, with monodisperse and narrow size distributions, is good for the next step synthesizing $ZnFe_2O_4$-based hollow nanospheres.

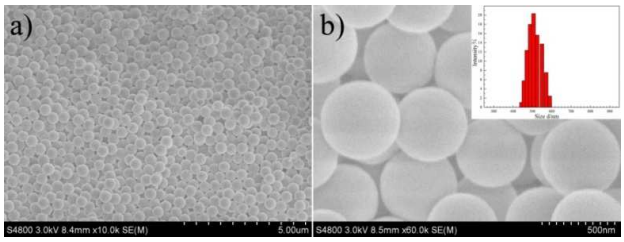

Figure 4. a),b) SEM images of PFS nanospheres at different magnifications (Inset: photograph illustrating DLS bargraph of the PFS nanospheres).

Figure 5 shows the representative SEM and TEM images of the $ZnFe_2O_4$ hollow nanospheres. The monodispersed $ZnFe_2O_4$ hollow nanospheres with narrow size distributions are demonstrated by SEM (Figure 5a). The magnified image (Figure 5b) indicates that the surface of the hollow nanospheres prepared at this condition is coarse and broken. We note that some hollow spheres had opening, which might be the imprint from the template removal. Because the shells of the hollow spheres are very thin, we could also observe some wrinkles on the hollow spheres. Compared with the original size of template spheres, the size of the resultant hollow spheres is about 230 nm, which is reduced to about 55 %. This reduction mainly depends on the shrinkage of template sphere due to further carbonization of organic matters and the densification of adsorbed metal ions to form $ZnFe_2O_4$ during the thermal treatment. TEM image of $ZnFe_2O_4$ is shown in Figure 5c, which exhibits a common hollow structure. And we could also estimate that the nanospheres diameter size and the shell thicknesses are about 230 nm and 15 nm, respectively, which are good consistent with SEM images of $ZnFe_2O_4$. SEM and TEM images of $ZnO/ZnFe_2O_4$ and $Fe_2O_3/ZnFe_2O_4$ hollow nanospheres are showed in Figures S1 (Figures S1 in the Supporting Information). From figure 5, we can easily conjecture the thin shell structure with high surface area possess many pores, which may serve as the transport paths for small molecules or allow the transmission and multiflections of visible light within their interior cavities, so as to endow thin shell with greatly enhanced photocatalytic activities [20].

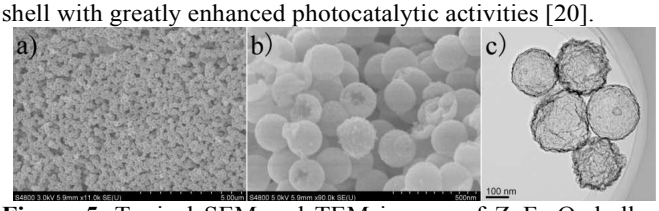

Figure 5. Typical SEM and TEM images of $ZnFe_2O_4$ hollow nanospheres: (a) Overall morphology SEM image of $ZnFe_2O_4$; (b) the close-up SEM image of $ZnFe_2O_4$; (c) TEM image of $ZnFe_2O_4$.

3.5 Optical absorption analysis

The optical properties of $ZnFe_2O_4$-based hollow nanospheres were probed by UV-visible diffuse reflectance spectroscopy as shown in Figure 6. The three samples show intense absorption in a wide wavelength range from UV to visible light with absorption tail extending into infrared region. And the absorption edge of $ZnFe_2O_4$-based composite is from 580 to 670 nm, which is favor for light absorption of photocatalyst [21]. The absorption band has no structures such as shoulders and possesses relatively steep edges, implying that the absorption shoulder of the ferrite in the visible region may be attributed to the electron excitation from the O-2p level into the Fe-3d level for spinel-type composite [22]. And there is an obvious enhancement in the visible light absorption of the S2 and S3, compared to the S1 sample. This property might have a positive contribution to the photocatalytic reactions, because a more efficient utilization of the solar energy could be achieved, and the colour of $ZnFe_2O_4$-based samples is consistent with the brick red color, as show in illustration of Figure 6 [23]. Furthermore, plots of $(\alpha h\nu)^2$ versus photo energy (eV) are illustrated in illustration of Figure 6, the band gap for S1, S2 and S3 is 1.84 eV, 1.88 eV and 1.81 eV, respectively.

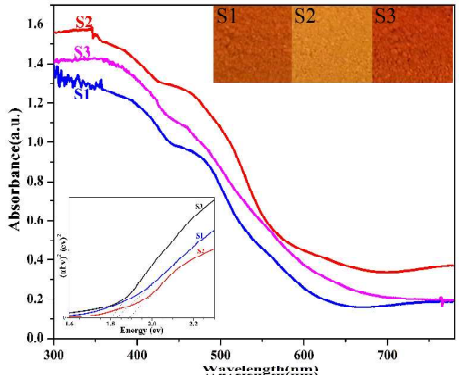

Figure 6. UV-visible diffuse reflectance spectra of $ZnFe_2O_4$-based hollow nanospheres: (S1) $ZnFe_2O_4$, (S2) $ZnO/ZnFe_2O_4$, (S3) $Fe_2O_3/ZnFe_2O_4$ (Inset: photograph illustrating actual color of the S1, S2, S3, respectively).

3.6 Transient photocurrent-time performance of the catalysts

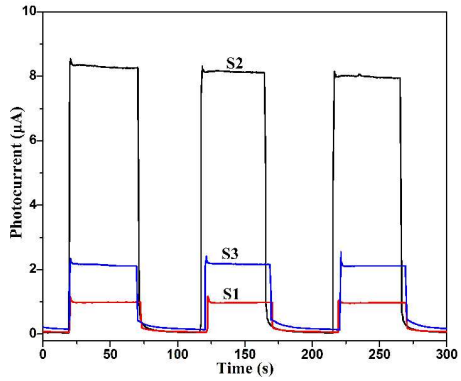

Figure 7. Photocurrent generation on $ZnFe_2O_4$-based hollow nanospheres electrode under visible light: (S1) $ZnFe_2O_4$, (S2) $ZnO/ZnFe_2O_4$, (S3) $Fe_2O_3/ZnFe_2O_4$.

To study the photocurrent response of the electrodes under visible light irradiation, the photocurrent-time measurements were measured in 1 M NaOH electrolytes under xenon lamp irradiation with 300 W, as shows in Figure 7. It can be seen clearly that both the S1, S2 and S3 electrodes demonstrate a rapid photocurrent response, when the visible-light illumination is on and off. Under illumination both of the photocurrent values remain constant. S2 and S3 electrode shows a considerably enhanced photocurrent density compared with the S1 electrode, and the photocurrent intensity of the S2 and S3 electrode is about four times and two times than that of the S1

electrode, respectively. In general, the higher generation of photocurrent might result from a better electron transfer rate between the two materials, so that the photogenerated electrons are more easily to form a greater current in the external electric field. In our experiment, the photocurrent enhancement of the S2 and S3 indicates an enhanced photoinduced electrons and holes separation, which could be attributed to the synergetic effect of $ZnFe_2O_4$ with the ZnO or Fe_2O_3 semiconductor.

3.7 PL analysis

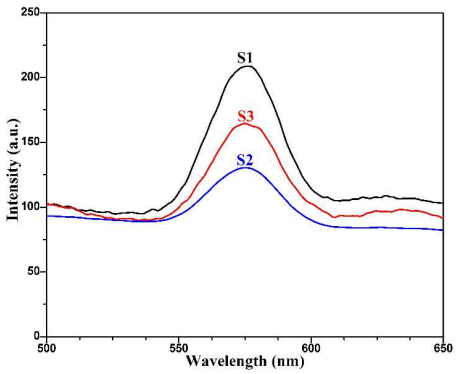

Figure 8. PL spectrum of as-prepared $ZnFe_2O_4$-based hollow nanospheres: (S1) $ZnFe_2O_4$, (S2) $ZnO/ZnFe_2O_4$, (S3) $Fe_2O_3/ZnFe_2O_4$.

PL emission spectrum is useful to disclose the migration, transfer, and recombination processes of the photogenerated electron-hole pairs in the semiconductors. PL emission mainly results from the recombination of excited electrons and holes. Thus, a weaker PL intensity represents a lower recombination probability of the electron-hole under light irradiation. Figure 8 shows the comparison of the PL spectra of $ZnFe_2O_4$-based hollow nanospheres, and the PL emission spectra of different samples excitation at 325 nm were examined. It is found that the PL emission spectra of the $ZnFe_2O_4$-based hollow nanospheres photocatalysts show the main peaks at near similar positions but with different intensities, and have a green-yellow emission near 575 nm, which is originated from near band-edge emission, namely the free excitons recombination through an excition-excition collision process. There is a significant decrease in the intensity of PL spectrum of S2 and S3 compared to that of S1. It indicates that the heterojunction construction could effectively inhibit the recombination of photogenerated charge carriers, which is helpful for the separation of photogenerated electron-hole pairs in S2 and S3 [24].

3.8 Photocatalytic activity

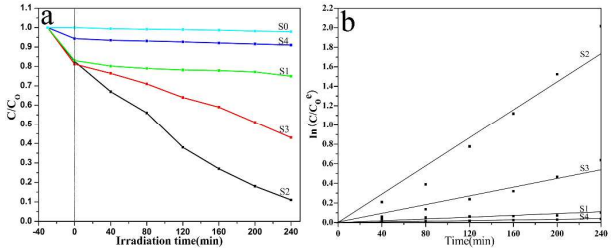

Figure 9. (a) Photocatalytic degradation of RhB in the presence of (S0) blank (without photocatalysts), (S1) $ZnFe_2O_4$, (S2) $ZnO/ZnFe_2O_4$, (S3) $Fe_2O_3/ZnFe_2O_4$, (S4) bulk $ZnFe_2O_4$; (b) Kinetic linear simulation curves of RhB degradation with different photocatalysts: (S1) $ZnFe_2O_4$, (S2) $ZnO/ZnFe_2O_4$, (S3) $Fe_2O_3/ZnFe_2O_4$, (S4) bulk $ZnFe_2O_4$.

In order to survey the effect of heterojunction construction, when coupling Fe_2O_3, ZnO with $ZnFe_2O_4$, a series of detailed contrast experiments are carried out from measuring the degradation efficiency of RhB aqueous solution under visible light irradiation. As shows in Figure 9a, the blank test shows that RhB cannot be degraded under visible light irradiation without photocatalysts, which indicates that the RhB has high structural stability. The adsorption rates of RhB solution for S1, S2, S3 and S4 in the dark is 16.9-18.8 % and 5.3 %, respectively. It can be found that the $ZnFe_2O_4$-based hollow nanospheres have stronger adsorption capacity compared to counterparts of bulk $ZnFe_2O_4$ for RhB, due to larger specific surface, as shows in Figure S2 and Table S1, the Brunauer-Emmett-Teller (BET) specific surface area of S1, S2, S3 and S4 is 95.8-98.2 m^2/g and 13.5 m^2/g, respectively (Figure S2 and Table S1 in the Supporting Information). Although the absorption data of $ZnFe_2O_4$-based hollow nanospheres are similar, their photocatalytic activities of samples are different, implying that the influence of adsorption is ignored in photocatalytic reaction. And it is observed that S4 is almost photocatalytic inactive and only 9.0% of RhB is converted in 4 h. On the contrary, 23.2% of RhB is converted over irradiated S1 hollow nanospheres in 4 h. Moreover, coupling $ZnFe_2O_4$ to ZnO or Fe_2O_3 as photocatalysts led to an obviously enhanced photocatalytic activity, and the corresponding degradation rates of RhB reached about 56.8% and 89.1%, respectively, after 4 h of visible-light irradiation. The result makes clear that heterojunction construction plays an important role in the enhanced photocatalytic activity.

For a better comparison of the photocatalytic activity of obtained photocatalysts, the kinetic model for degradation of RhB aqueous solution is discussed. The relevant equation is listed as below: $\ln(C/C^e_o)=-\kappa_{app} * t$, where C^e_o and C is the concentration of the dyes at adsorption-desorption equilibrium and after various intervals of time, and κ is the apparent first-order rate constant (min^{-1}). The κ value is obtained from the gradient of the graph of $\ln (C/C^e_o)$ versus time (min), which is shown in Figure 9b. The reaction rate constant κ for the photocatalyzed degradation of RhB with the S1, S2, S3 and S4 is 0.000468, 0.00742, 0.00229 and 0.000167 min^{-1}, respectively. It can be observed that the κ value of S2 and S3 is higher than the others, and is over ten times and four times faster than that of S1, which is in accordance with the curves of the catalysts' photocatalytic activities.

3.9. Circulation experiment and magnet separation

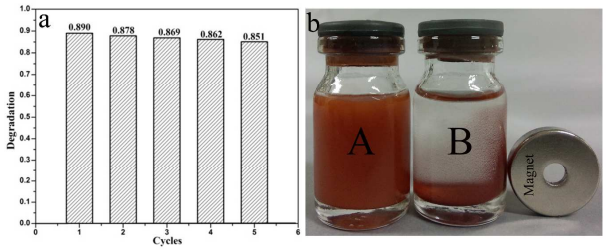

Figure 10. (a)Reuse of the $ZnO/ZnFe_2O_4$ photocatalyst; (b) $ZnO/ZnFe_2O_4$ photocatalyst collected by an external magnet: (A) Before separated, (B) After separated.

In view of practical application, the photocatalyst should be chemically and optically stable after several repetitive tests. The circulating runs in the photocatalytic degradation of RhB in the presence of $ZnO/ZnFe_2O_4$ under visible light are checked, as showes in figure 10a. After five recycles, the photocatalytic efficiency of the $ZnO/ZnFe_2O_4$ hollow nanospheres decreased by only 3.9%, which indicates that the obtained $ZnFe_2O_4$-based composites are highly stable [25]. We are interested in the reasons for $ZnO/ZnFe_2O_4$ with high stability of photocatalyst activity after several repetitive tests. Because $ZnO/ZnFe_2O_4$ is the most stable iron oxide under ambient conditions. And $ZnO/ZnFe_2O_4$ hollow nanospheres with low density and fluffy structure exist in plenty of large volume pores in this structure, which can be considered as spacious transport paths for the RhB molecules. Reactant molecules cannot block the reactive sites on the framework walls and affect transmission reflections of light within the interior cavity. What are the reasons for the decrease of photocatalytic efficiency, after several circulation. We think that there exists in the interaction between electrostatic interaction and coordination with surface hydroxyl groups or chemical reaction system, which makes some active site inactivation. Furthermore, the obtained $ZnO/ZnFe_2O_4$ composite photocatalysts can be easily recycled by external magnet, as clearly shows in figure 10b.

3.10 Mechanism on Enhancement

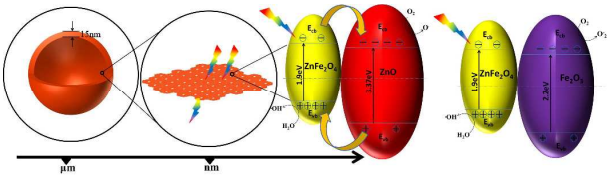

Figure 11. Schematic diagram showing the reasons for enhanced catalytic activity of $ZnFe_2O_4$-based hollow nanospheres.

The photocatalysis experimental results indicate $ZnO/ZnFe_2O_4$ and $Fe_2O_3/ZnFe_2O_4$ hollow nanospheres show a much higher catalytic activity than that of $ZnFe_2O_4$ hollow nanospheres and bulk $ZnFe_2O_4$, which can be ascribed to the formation of the heterostructure. Taking $ZnO/ZnFe_2O_4$ nanoparticles as an example explain the increased photocatalytic activity, as shown in Figure 11. Under visible light irradiation, the electrons in the VB of $ZnFe_2O_4$ are excited to its CB. Thereby the VB of $ZnFe_2O_4$ is rendered partially holes. Due to the VB level $ZnFe_2O_4$ is lower by 1.5 V than that of ZnO, thus holes in the VB of ZnO can be transferred to that of $ZnFe_2O_4$ [26]. Simultaneously, $ZnFe_2O_4$ is used mainly as a hole-accepting semiconductor. As a result, the semiconductors with matching band potentials are tightly bonded to construct the efficient heterostructure. The migration of photogenerated carriers can be promoted by the internal field, so less of a barrier exists. Therefore, the probability of electron-hole recombination can be reduced, and the result is consistent with Figure 9. A larger number of electrons on the ZnO surface and holes on the $ZnFe_2O_4$ surface, respectively, can participate in photocatalytic reactions to directly or indirectly mineralize organic pollution, and thus the photocatalytic reaction can be enhanced greatly. This is also supported by the fact that the photocatalytic activity of $Fe_2O_3/ZnFe_2O_4$ can be greatly improved by coupling $ZnFe_2O_4$ to Fe_2O_3.

The hollow nature of the as-prepared $ZnFe_2O_4$-based hollow nanospheres is also responsible for its superior photocatalytic performance. The improvement of the catalytic activity due to the existence of the hollow morphology has been previously reported [27]. Especially in photocatalysis, such a thin shell structure only 15 nm can serve as the transport paths for small molecules or allow the transmission and multiflections of visible light within their interior cavities, and also reduce the recombination opportunities of the photogenerated electron-hole pairs, which could move effectively to the surface to degrade the absorbed RhB molecules [28,29].

However, we are more interested in is that $ZnO/ZnFe_2O_4$ hollow nanospheres show a much higher catalytic activity than $Fe_2O_3/ZnFe_2O_4$ hollow nanospheres. ZnO is a wide bandgap semiconductor material relative to Fe_2O_3. When couple $ZnFe_2O_4$ to ZnO or Fe_2O_3 as photocatalysts, electrons in $ZnFe_2O_4$ transferring to Fe_2O_3 is easier recombination than that to ZnO, and which is consistent with the PL intensity of $ZnO/ZnFe_2O_4$ hollow nanospheres lower than $Fe_2O_3/ZnFe_2O_4$ hollow nanospheres. Since the heterojunction construction of $ZnO/ZnFe_2O_4$ and $Fe_2O_3/ZnFe_2O_4$ possesses unique optical and electronic properties, $ZnO/ZnFe_2O_4$ exhibits a stronger absorption in the visible region compared to $Fe_2O_3/ZnFe_2O_4$, and the photocurrent intensity of $ZnO/ZnFe_2O_4$ electrode is higher that of $Fe_2O_3/ZnFe_2O_4$ electrode. So we can draw that the catalytic activity of $ZnO/ZnFe_2O_4$ is higher than that of $Fe_2O_3/ZnFe_2O_4$ by the above conclusions.

4. Conclusions

In summary, we report a general method applicable to the synthesis of $ZnFe_2O_4$-based hollow nanospheres via impregnating-calcination process using PFS as template. $ZnFe_2O_4$, $ZnO/ZnFe_2O_4$ and $Fe_2O_3/ZnFe_2O_4$ composite were prepared by adjusting the amounts of zinc salts. The average diamete of $ZnFe_2O_4$-based hollow nanospheres is about 230 nm and possesses a shell with the thickness of about 15 nm. The photocatalysis experimental results indicate that $ZnO/ZnFe_2O_4$ and $Fe_2O_3/ZnFe_2O_4$ composites show a much higher catalytic activity than $ZnFe_2O_4$ and bulk $ZnFe_2O_4$ composites, which can ascribed to the high surface area, thin shell thicknesses, and matching heterostructure. And the improved performance

observed over the $ZnO/ZnFe_2O_4$ composite compared to $Fe_2O_3/ZnFe_2O_4$ hollow nanospheres can be ascribed to possession of unique optical and electronic properties, such as $ZnO/ZnFe_2O_4$ compared to $Fe_2O_3/ZnFe_2O_4$ with lower electrons recombination, stronger absorption of visible light and higher photocurrent intensity. The $ZnFe_2O_4$-based hollow nanospheres are highly stable after five recycles, and could be conveniently separated by using an external magnetic field. The study also provides an easy and effective method in the fabrication of composition with a sound heterojunction that may be useful to design novel high-performance photocatalysts.

Acknowledgements

This work was financially supported by the National Natural Science Foundation of China (NO. 51202136), Special Fund from Shaanxi Provincial Department of Education (2013JK0939), the Academic Backbone Cultivation Program of Shaanxi University of science & technology (XSGP201202) and the Postgraduate Innovation Fund of Shaanxi University of Science and Technology.

References

[1] B. B. Li, Z. B. Zhao, F. Gao, X. Z. Wang, J. S. Qiu, Appl. Catal. B, 2014, **147**, 958.
[2] Z. M. Li, X. Y. Lai, H. Wang, D. Mao, C. j. Xing, D. Wang, J. Phys. Chem. C, 2009, **113**, 2792.
[3] G. P. Li, L. Q. Mao, RSC Advances, 2012, **2**, 5108.
[4] A. Wilson, S. R. Mishra, R. Gupta, K. Ghosh, J. Magn. Magn. Mater. 2012, **324**, 2597.
[5] S. W. Cao, Y. J. Zhu, G. F. Cheng, Y. H. Huang, Journal of Hazardous Materials 2009, **171**, 431.
[6] H. H. Qian, Y. Hu, Z. Q. Li, X. Y. Yang, L. C. Li, X. T. Zhang, R. Xu, J. Phys. Chem. C, 2010, **114**, 17455.
[7] A. A. Tahir a, H. A. Burch, K.G. Upul Wijayantha, B. G. Pollet, International journal of hydrogen energy, 2013, **38**, 4315.
[8] X. Y. Li, Y. Hou, Q. D. Zhao, W. Teng, X. J. Hu, G. H. Chen, Chemosphere, 2011, **82**, 581.
[9] J. Y. Cao, J. J. Xing, Y. J. Zhang, H. Tong, Y. P. Bi, T. Kako, M. Takeguchi, J. H. Ye, Langmuir, 2013, **29**, 3116.
[10] J. Yin, L. J. Bie, Z. H. Yuan, Materials Research Bulletin, 2007, **42**, 1402.
[11] S. H. Xu, D. L. Feng, W. F. Shangguan, J. Phys. Chem. C, 2009, **113**, 2463.
[12] T. P. Xie, L. J. Xua, C. L. Liu, Y. Wang, Applied Surface Science, 2013, **273**, 684.
[13] L. Zhang, Y. M. He, P. Ye, Y. Wu, T. H. Wu, Journal of Alloys and Compounds, 2013, **549**, 105.
[14] D. Q. He, L. L. Wang, D. D. Xu, J. L. Zhai, D. J. Wang, T. F. Xie, Appl. Mater. Interfaces, 2011, **3**, 3167.
[15] Y. L. Tian, B. B. Chang, J. L. Lu, J. Fu, F. N. Xi, X. P. Dong, Appl. Mater. Interfaces 2013, **5**, 7079.
[16] C. H. Miao, S. L. Ji, G. P. Xu, G. D. Liu, L. D. Zhang, C. H. Ye, Appl. Mater. Interfaces, 2012, **4**, 4428.
[17] J. Liu, S. Z. Qiao, H. Liu, J. Chen, A. Orpe, D. Y. Zhao, G. Q. Lu, Angew. Chem. Int. Ed., 2011, **50**, 5947.
[18] S. Ito, P. Chen, P. Comte, M. K. Nazeeruddin, P. Liska, P. Pechy, M. Gratzel, Res. Appl., 2007, **15**, 603.
[19] X. M. Sun, J. F. Liu, Y. D. Li, Chemistry-A European Journal, 2006, **12**, 2039.
[20] X. N. Li, R. K. Huang, Y. H. Hu, Y. J. Chen, W. J. Liu, R. S. Yuan, Z. H. Li, American Chemical Society, 2012, **51**, 6245.
[21] L. Sun, R. Shao, L. Q Tang, Z. D. Chen, Journal of Alloys and Compounds, 2013, **564**, 55.
[22] M. H. Sua, C. Hea, V. K. Sharmab, M. A. Asi, D. Xia, X. Z. Li, H. Q. Deng, Y. Xiong, Journal of Hazardous Materials, 2012, **211-212**, 95.
[23] H. G. Kim, P. H. Borse, J. S. Jang, E. D. Jeong, O. S. Jung, Y. J. Suhd, J. S. Lee, Chem. Commun., 2009, 5889.
[24] G. K. Fu, G. N. Xu, S. P. Chen, L. Lei, M. L. Zhang, Catalysis Communications, 2013, **40**, 120.
[25] R. Shao, L. Sun, L. Q. Tang, Z. D. Chen, Chemical Engineering Journal, 2013, **217**, 185.
[26] D. B. Lu, Y. Zhang, S. X. Lin, L. T. Wang, C. M. Wang, Journal of Alloys and Compounds, 2013, **579**, 336.
[27] S. Mandal, M. Sathish, G. Saravanan, K. K. R. Datta, Q. M. Ji, J. P. Hill, H. Abe, I. Honma, K. J. Ariga, Am. Chem. Soc., 2010, **132**, 14415.
[28] X. X. Yu, S. W. Liu, J. G. Yu, Appl. Catal., B, 2011, **104**, 12.
[29]W. Chen, Z. G. Wang, Z. J. Lin, L. Y. Lin, Journal of Applied Physics, 1997, **82**, 3111.